Large eddy simulation of shock wave/turbulent boundary layer interaction under incipient and fully separated conditions ⊘

Ji Xiangxin (纪相鑫) ID ; Li Xinliang (李新亮) ID ; Tong Fulin (童福林) ID ; Yu Changping (于长平) ✉ ID

Check for updates

View Online

Export Citation

AIP Publishing

Large eddy simulation of shock wave/turbulent boundary layer interaction under incipient and fully separated conditions

View Online   Export Citation   CrossMark

Xiangxin Ji (纪相鑫),[1,2] (iD) Xinliang Li (李新亮),[1,2] (iD) Fulin Tong (童福林),[3] (iD) and Changping Yu (于长平)[1,a] (iD)

AFFILIATIONS

[1]LHD, Institute of Mechanics, Chinese Academy of Sciences, Beijing 100190, China
[2]School of Engineering Science, University of Chinese Academy of Sciences, Beijing 100049, China
[3]State Key Laboratory of Aerodynamics, Mianyang 621000, China

[a]Author to whom correspondence should be addressed: cpyu@imech.ac.cn

ABSTRACT

Large eddy simulations of shock wave/turbulent boundary layer interaction on a compression ramp at the Mach number $Ma_\infty = 5$ and Reynolds number $Re_\infty = 14\,000$ are performed to investigate the impact of the incipient and fully separated conditions on the development of the flow field. The quasi-dynamic subgrid-scale kinetic energy equation model, which combines the benefits of the gradient model with the eddy-viscosity model, has been applied. Compared with the previous experimental and numerical results, the simulation was validated. The flow structures, turbulence properties, vortex structures, and low-frequency unsteadiness are all investigated. The flow field of the incipient separation is attached and rarely impacted by shock. An evident separation bubble and localized high wall temperatures in fully separated flow are caused by the separation shock's significant reverse pressure gradient. The Reynolds stress components exhibit significant amplification in both cases, and the peak outward shifts from the near-wall region to the center of the free shear layer. Turbulent kinetic energy terms were analyzed, and the two scenarios show a significant difference. The power spectral density of the wall pressure fluctuations shows that the low-frequency motion of the incipient separation is not apparent relative to the fully separated flow.

Published under an exclusive license by AIP Publishing. https://doi.org/10.1063/5.0147829

I. INTRODUCTION

Shock wave/turbulent boundary layer interaction (STBLI) widely exists in the internal and external flow of aircraft, missiles, rockets, and other related weapon projectiles. It will cause flow separation, strong pressure fluctuations, and local peak heat flow in the flow field, affecting the aerodynamic performance of the aircraft.[1] In the past few decades, many researchers have carried out theoretical, experimental, and numerical research on the STBLI and achieved very significant results.[2–8] However, many problems still need to be fully solved, such as the mechanism of low-frequency unsteadiness of STBLI, the overshoot of the skin-friction coefficient, and the turbulence amplification.[9,10] Therefore, it is essential to study the STBLI problem further.

The strong reverse pressure gradient due to the strong shock wave interaction will cause the flow field to separate, thereby changing the flow state. Simpson divides the separation flow into incipient detachment (ID), intermittent transitory detachment (ITD), transitory detachment, and detachment based on the fraction of time that the

flow moves downstream.[11,12] Wu and Martín[13] performed direct numerical simulation (DNS) studies of a Mach number of 24° compression corner to analyze the shock motion in fully separated flow. The results show that the shock and spanwise mean separation point undergo low-frequency unsteadiness. Tong *et al.*[14] studied the turning angle effects of compression corner by turbulent kinetic energy (TKE) budgets and found that the influence of shear layer above the separation bubble on the mechanism is significant. John and Kulkarni[15] studied the effect of leading edge bluntness ramp interaction. The laminar boundary layer results show that the increase in separation bubble size has been observed with an increase in the leading edge radius until the "inversion radius." Duan *et al.*[16] investigated the shock interactions at two different heights between the compression and decompression corners. The results show that the size of the separation region is significantly decreased in the lower case. Xie *et al.*[17] studied the characteristics and its variation with Reynolds number in expansion—compression corner. Zhang *et al.*[18] conducted a DNS of swept compression ramp STBLI. They found that the spanwise variation of

the shock wave inclination induced the peak friction and heating increase along the spanwise direction.

The low-frequency unsteadiness of shock is also a critical problem in STBLI. Beresh et al.[19] used particle image velocimetry (PIV) to study the compression corner configuration at Mach 5, and they believe that a fuller velocity profile will increase the resistance to separation, resulting in a reduction in separation bubble and ultimately causing the separation shock move downstream. Ganapathisubramani observed elongated streamwise strips of uniform low and high speed fluid with length greater than 8δ in the Mach 2 turbulent boundary layer near-wall region, namely "superstructures."[20] Their subsequent work suggested that the superstructures may be responsible for the low-frequency unsteadiness.[21] Pirozzoli and Grasso[22] suggested that an acoustic feedback mechanism in the interaction may cause low-frequency unsteadiness. Piponniau et al.[23] proposed a mechanism based on the shear layer entrainment of fluids. The dynamic mode decomposition (DMD) analysis results of Priebe et al.[24] suggest that Görtler vortices may be responsible for the unsteady motion of separation shock. Waindim et al.[25] found that the shedding of the Kelvin–Helmholtz structure is closely related to the collapse of the separation bubble, supporting the separation flow driven by the low-frequency unsteadiness. Hu et al.[6,26] used large eddy simulation (LES) to study the low-frequency unsteady motions of the backward-facing step and forward-facing step, and they found that the Görtler-like vortices are strongly correlated with the low-frequency unsteadiness. Li et al.[27] proposed a new method for judging the Görtler vortices.

Recently, scholars have also made progress in other unsolved problems. Combs et al.[28] used experiments to investigate STBLI at different Mach numbers. Proper orthogonal decomposition (POD) results show that low Mach numbers have higher energy in low-order modes, while high Mach numbers have a more uniform energy distribution. They also reproduced the entire shock breathing cycle by DMD analysis. Zhou et al.[29] investigated the separation vortex in the swept STBLI by experiments and numerical simulation. The results show that the Mach number has little effect on the height of the separation vortex core but has a greater effect on the size of the separation vortex and the growth rate of the separation vortex intensity. Tonicello et al.[30] studies the large-scale kinetic energy equation. Based on such equations, they performed a 24° compression/expansion ramp STBLI. They found that the compression motions can promote the forward transfer of kinetic energy down the energy cascade, whereas expansion regions are more likely to experience a backscatter of kinetic energy. Shi and Yan[31] proposed that the main reasons for the turbulence amplification are the shear effects and the flow deceleration/acceleration. Tong et al.[7,32–34] studied the wall heat flux and the skin friction through decomposition, and they found that the shock interaction will amplify the large scale structures in the outer region. Jiang et al.[35] used Helmholtz decomposition to study the effect of compressibility in STBLI. Lai et al.[36] identified the effects of shock impingement on the behavior of bump flow. Guo et al.[37] applied convergent–divergent riblets to control the STBLI.

Previous scholars have achieved many results in the STBLI. However, there are fewer studies on incipient separation and fully separated flow in hypersonic. Therefore, this paper will study the effect of incipient and fully separated conditions on STBLI. The remainder of this paper is organized as follows: The simulation methods are briefly described in Sec. II. Section III analyzes the results with an emphasis on flow characteristics and turbulence properties. The conclusions are presented in Sec. IV.

II. SIMULATION METHODS

The compressible Navier–Stokes equation after filtering takes the form

$$\frac{\partial \bar{\rho}}{\partial t} + \frac{\partial \bar{\rho}\widetilde{u}_j}{\partial x_j} = 0, \tag{1}$$

$$\frac{\partial \bar{\rho}\widetilde{u}_i}{\partial t} + \frac{\partial \bar{\rho}\widetilde{u}_i\widetilde{u}_j}{\partial x_j} = -\frac{\partial \bar{p}}{\partial x_i} + \frac{\partial \widetilde{\sigma}_{ij}}{\partial x_j} - \frac{\partial \tau_{ij}}{\partial x_j}, \tag{2}$$

$$\frac{\partial \bar{\rho}\widetilde{E}}{\partial t} + \frac{\partial (\bar{\rho}\widetilde{E} + \bar{p})\widetilde{u}_j}{\partial x_j} = -\frac{\partial \widetilde{q}_j}{\partial x_j} + \frac{\partial \widetilde{\sigma}_{ij}\widetilde{u}_i}{\partial x_j} - \frac{\partial C_p Q_j}{\partial x_j} - \frac{\partial J_j}{\partial x_j}, \tag{3}$$

where

$$\bar{p} = \bar{\rho}R\widetilde{T}, \tag{4}$$

$$\tau_{ij} = \bar{\rho}(\widetilde{u_i u_j} - \widetilde{u}_i\widetilde{u}_j), \tag{5}$$

$$\widetilde{\sigma}_{ij} = 2\mu(\widetilde{T})\left(\widetilde{S}_{ij} - \frac{1}{3}\delta_{ij}\widetilde{S}_{kk}\right), \tag{6}$$

$$\widetilde{S}_{ij} = \frac{1}{2}\left(\frac{\partial \widetilde{u}_i}{\partial x_j} + \frac{\partial \widetilde{u}_j}{\partial x_i}\right), \tag{7}$$

$$\mu = \frac{1}{\mathrm{Re}}\left(\frac{\widetilde{T}}{\widetilde{T}_\infty}\right)^{3/2}\frac{\widetilde{T}_\infty + 110.3}{\widetilde{T} + 110.3}, \tag{8}$$

$$\bar{\rho}\widetilde{E} = \bar{\rho}C_v\widetilde{T} + \frac{1}{2}\bar{\rho}\widetilde{u}_i\widetilde{u}_i + \bar{\rho}k_{sgs}, \tag{9}$$

$$\bar{\rho}k_{sgs} = \frac{1}{2}\bar{\rho}(\widetilde{u_i u_i} - \widetilde{u}_i\widetilde{u}_i), \tag{10}$$

$$\widetilde{q}_j = \frac{C_p\mu(\widetilde{T})}{P_r}\frac{\partial \widetilde{T}}{\partial x_j}, \tag{11}$$

$$Q_j = \bar{\rho}\left(\widetilde{u_j T} - \widetilde{u}_j\widetilde{T}\right), \tag{12}$$

$$J_j = \frac{1}{2}\bar{\rho}\left(\widetilde{u_i u_i u_j} - \widetilde{u_i u_i}\widetilde{u}_j\right). \tag{13}$$

The compressible subgrid-scale (SGS) kinetic energy equation can be written as

$$\frac{\partial \bar{\rho}k_{sgs}}{\partial t} + \frac{\partial \bar{\rho}k_{sgs}\widetilde{u}_j}{\partial x_j} = -\Pi_\Delta - \frac{\partial J_j}{\partial x_j} - \varepsilon_s - \varepsilon_d$$
$$+ \Pi_p + \frac{\partial \zeta_j}{\partial x_j} + \frac{\partial \left[\mu(\widetilde{T})\frac{\partial k_{sgs}}{\partial x_j}\right]}{\partial x_j}, \tag{14}$$

where

$$\Pi_\Delta = \tau_{ij}\frac{\partial \widetilde{u}_i}{\partial x_j}, \tag{15}$$

$$\varepsilon_s = 2\mu(\widetilde{T})\left(\widetilde{\mathbb{S}_{ij}\mathbb{D}_{ij}} - \widetilde{\mathbb{S}}_{ij}\widetilde{\mathbb{D}}_{ij}\right), \tag{16}$$

$$\mathbb{D}_{ij} = \frac{\partial u_i}{\partial x_j} - \frac{1}{3}\delta_{ij}\frac{\partial u_k}{\partial x_k}, \tag{17}$$

$$\varepsilon_d = \frac{\partial}{\partial x_j}\left[\frac{5}{3}\mu(\widetilde{T})\left(\widetilde{u_j\frac{\partial u_k}{\partial x_k}} - \widetilde{u}_j\frac{\partial \widetilde{u}_k}{\partial x_k}\right)\right], \tag{18}$$

$$\Pi_P = \overline{p\frac{\partial u_k}{\partial x_k}} - \bar{p}\frac{\partial \widetilde{u}_k}{\partial x_k}, \tag{19}$$

$$\zeta_j = \tau_{ij}\widetilde{u}_i + \mu(\widetilde{T})\frac{\partial}{\partial x_i}\left(\frac{\tau_{ij}}{\bar{\rho}}\right) + RQ_j. \tag{20}$$

The spatial filtering with a low-pass filter at scale Δ of a generic variable φ is denoted as $\bar{\varphi}$, and the corresponding density-weighted (Favre) filtering $\widetilde{\varphi}$ ($\widetilde{\varphi} = \overline{\rho\varphi}/\bar{\rho}$). The ρ, u_i, p, T, σ_{ij}, and E are the density, velocity, pressure, temperature, viscous stress, and total energy, respectively. The P_r is the molecular Prandtl number, the μ is the molecular viscosity, and R is the specific gas constant. The k_{sgs}, τ_{ij}, Q_j, q_j, J_j, Π_Δ, ε_s, ε_d, and Π_p are the subgrid-scale (SGS) kinetic energy, the SGS stress, the SGS heat flux, the heat flux, the SGS diffusion term, the SGS energy flux, the solenoidal dissipation, the dilatational dissipation, and the pressure dilatation, respectively.

A quasi-dynamic subgrid-scale kinetic energy equation model (QKM) has been applied, which combines the merits of the eddy-viscosity model and the gradient model, and the local coefficients of the model are determined dynamically. Many simulations demonstrate the model's strong numerical robustness and excellent accuracy, including those of compressible turbulent channel flow, compressible flat-plate boundary layer, and spherical converging Richtmyer–Meshkov instability.[38]

In QKM, the SGS stress can be expressed as

$$\tau_{ij}^{mod} = -2C_{sm}\bar{\rho}\Delta^2|\widetilde{S}|\widetilde{\mathbb{S}}_{ij} + \frac{2}{3}\delta_{ij}\bar{\rho}k_{sgs}, \tag{21}$$

where

$$|\widetilde{S}| = \sqrt{2\widetilde{S}_{ij}\widetilde{S}_{ij}}, \tag{22}$$

$$C_{sm} = -\frac{\left(C_0\Delta_k^2\bar{\rho}\frac{\partial\widetilde{u}_i}{\partial x_k}\frac{\partial\widetilde{u}_j}{\partial x_k} - \frac{2}{3}\delta_{ij}\bar{\rho}k_{sgs}\right)\widetilde{S}_{ij}}{2\bar{\rho}\Delta^2|\widetilde{S}|\widetilde{\mathbb{S}}_{ij}\widetilde{S}_{ij}}, \tag{23}$$

$$C_0 = \frac{2k_{sgs}}{\Delta_l^2\frac{\partial\widetilde{u}_k}{\partial x_l}\frac{\partial\widetilde{u}_k}{\partial x_l}}. \tag{24}$$

The SGS heat flux can be expressed as

$$Q_j^{mod} = -\frac{\mu_{sgs}}{Pr_{sgs}}\frac{\partial\widetilde{T}}{\partial x_j}, \tag{25}$$

where Pr_{sgs} is the SGS Prandtl number, and it can be solved in the QKM as

$$Pr_{sgs} = -\frac{\partial\left(\frac{\mu_{sgs}}{\bar{\rho}}\frac{\partial\widetilde{T}}{\partial x_j}\right)}{\frac{\partial\left(C_0\Delta_k^2\frac{\partial\widetilde{u}_j}{\partial x_k}\frac{\partial\widetilde{T}}{\partial x_k}\right)}{\partial x_j}}. \tag{26}$$

The pressure diffusion Π_p can be modeled as

$$\Pi_p \approx C_0\Delta_m^2\frac{\partial\bar{p}}{\partial x_m}\frac{\partial^2\widetilde{u}_k}{\partial x_m\partial x_k}. \tag{27}$$

The solenoidal dissipation ε_s can be modeled as

$$\varepsilon_s = 2C_0\Delta_k^2\mu(\widetilde{T})\frac{\partial\widetilde{\mathbb{S}}_{ij}}{\partial x_k}\frac{\partial\widetilde{\mathbb{D}}_{ij}}{\partial x_k}. \tag{28}$$

The dilatational dissipation ε_d can be modeled as

$$\varepsilon_d \approx \frac{5}{3}\frac{\partial}{\partial x_j}\left[C_0\Delta_l^2\mu(\widetilde{T})\frac{\partial\widetilde{u}_j}{\partial x_l}\frac{\partial^2\widetilde{u}_k}{\partial x_k\partial x_l}\right]. \tag{29}$$

A. Mesh and computational domains

Many researchers have studied the incipient separation mechanism in STBLI.[39–46] They found that the incipient separation at the compression corner is a gradual rather than an abrupt phenomenon.[39,40] Also, it is challenging to ascertain the incipient separation angle because doing so will result in different incipient separation angles when employing various experimental detection techniques.[41] Furthermore, the wall temperature, Mach number, and Reynolds number may influence the incipient separation angle.[44–46] Concerning the Mach 2.9 experiment, Settles $et\ al.$[39] found that the corner angle for incipient separation lies within a range of $15°$–$18°$. In contrast, Babinsky and Edwards[41] found a reversed flow in the corner when cylindrical flare angles of $10°$ and higher in the Ma5 experiment were present. When the Reynolds number is between 10^4 and 10^7 and the Mach number is 2.9, the incipient separation angle for an adiabatic wall is between $6.5°$ and $12°$.[42] In comparison, the effect of wall cooling was to raise the angle of incipient separation.[43] In general, giving a definite incipient separation angle is very difficult. However, according to the above conclusions, we can provide an angle that falls within the range of the incipient separation angle. Hence, based on the previous conclusions and combined with the current parameters, the present work selects $14°$ and $34°$ to represent the incipient and fully separated flow, respectively. The contours of mean streamwise velocity fields and the incipient and fully separated flow based on Simpson's criterion support the current configuration, as will be described later.

The computational domain of the $34°$ compression corner is sketched in Fig. 1, where the corner position is the origin of the coordinates. Note that x, y, and z represent the streamwise, wall-normal, and spanwise directions, respectively, and u, v, and w represent the velocity components in these three directions. The inlet of the computational domain is a laminar boundary layer, which is obtained by numerical simulation of the two-dimensional flat laminar boundary layer under the same inflow conditions. In order to make a fast transition from the laminar flow to turbulent flow, we apply the wall blowing and suction disturbance in the upstream flat plate x_a to x_b. Figure 2 shows a 2D grid schematic in the x–y plane, where the x and y directions are shown at ten grid point intervals. We use the algebraic analysis method to generate the grid. The x-direction grid is uniformly dense in the corner area, the y-direction grid is hyperbolically stretched to increase the resolution, and the z-direction grid is uniformly distributed. Detailed mesh information is shown in Table I.

For the first case, the compression corner is $14°$, and the computational mesh is $1930 \times 240 \times 260$ in the streamwise, wall-normal, and spanwise directions, respectively. For the second case, the compression corner is $34°$, and the mesh is $2500 \times 400 \times 300$. The computational domain for both cases is $L_y = 55$ mm in the wall-normal direction and $L_z = 24$ mm in the spanwise direction. The grid space in the streamwise, wall-normal, and spanwise directions are also
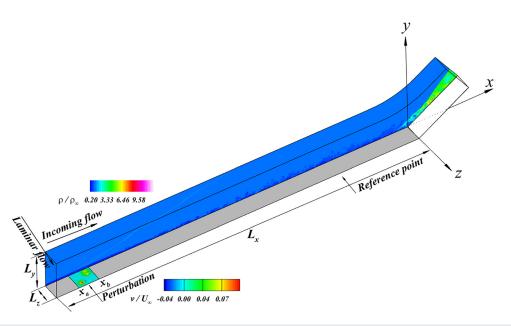
FIG. 1. Computational domain of 34° compression corner. The flow configuration is illustrated using the contour of the density ρ/ρ_∞ in the x–y plane at $z = 0$. The wall blowing and suction region are highlighted by the contour of the wall-normal velocity v between x_a and x_b. The corner inlet plane is denoted as reference point.
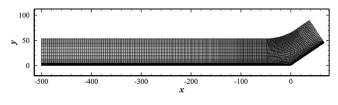

FIG. 2. Computational mesh of 34° compression corner in the x–y plane where the x direction and y direction are shown at ten grid points intervals.

shown in Table I, in which all grid spaces are normalized by the wall unit at $x = -100$ mm (the corner inlet plane). The Δy_w^+ represents the first grid above the wall in the wall-normal direction, and Δy_δ^+ represents grid space at the edge of boundary layer.

B. Numerical methods and simulation parameters

The Mach number of the incoming free-stream flow is $Ma_\infty = 5$. The incoming free-stream Reynolds number per unit millimeter is $Re_\infty = 14\,000$, the freestream temperature is $T_\infty = 79$ K, and the wall temperature $T_w = 294$ K. The subscript "∞" refers to the quantity in the free-stream flow.

The filtered Navier–Stokes (N–S) equations for compressible flows in LES [Eqs. (1)–(3)] is used. To enhance the robustness of the program and reduce nonphysical oscillations, we first converted the

TABLE I. Grid space for both cases.

Case	Grid	Δx^+	Δy_w^+	Δy_δ^+	Δz^+
14°	$1930 \times 240 \times 260$	12.37	0.62	5.96	5.71
34°	$2500 \times 400 \times 300$	9.27	0.37	3.58	4.93

numerical flux into characteristic space and then performed Steger-Warming split on the flux in characteristic space.[47] The inviscid terms are solved using a hybrid scheme with a modified Jameson shock sensor, an excellent way to solve complex problems.[48] The form of modified Jameson sensor is as follows:

$$\phi_i = \frac{|-p_{i-1} + 2p_i - p_{i+1}|}{p_{i-1} + 2p_i + p_{i+1}},$$
$$\phi_j = \frac{|-p_{j-1} + 2p_j - p_{j+1}|}{p_{j-1} + 2p_j + p_{j+1}},$$
$$\phi_k = \frac{|-p_{k-1} + 2p_k - p_{k+1}|}{p_{k-1} + 2p_k + p_{k+1}}, \quad (30)$$
$$\theta = \phi_i + \phi_j + \phi_k.$$

The thresholds are set θ_1 and θ_2. When $\theta \leq \theta_1$, it means the flow is smooth and sixth-order upwind scheme is used; when $\theta_1 \leq \theta \leq \theta_2$, it means the flow has weak discontinuities, and the seventh-order weighted essentially non-oscillatory (WENO) is used; when $\theta \geq \theta_2$, it means the flow has strong discontinuities, and shock waves, so the fifth-order WENO is used. In this paper, we set θ_1 and θ_2 as 0.02 and 0.1, respectively. The viscous flux terms are solved using an eighth-order central difference scheme. After all the spatial terms are solved, the third-order Runge–Kutta method is used for the temporal integration.[49] In this paper, the high-order finite-difference code (OpenCFD-SC) developed by Li is used.[50] Moreover, this code has been widely used in compression ramp and incident shock/wave boundary layer interaction, which shows high accuracy and reliability.[51,52]

C. Validation of incoming turbulent boundary layer

Figure 3 shows the van Direst transformed mean streamwise velocity in the corner inlet. The transformed velocity U_{vd}^+ conforms to
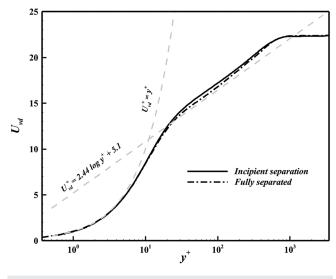
FIG. 3. Van Driest transformed mean streamwise velocity in the corner inlet.

the linear distribution law in the region of the viscous bottom layer, in the logarithmic law region in line with the logarithmic distribution law $\bar{U}_{vd}^{+} = 2.44 \log(y^{+}) + 5.1$. The transition region and the wake region are also clear.

Figure 4 shows the distribution of the root mean square of the three velocity components along the wall-normal direction in the corner inlet, which can show the intensity of turbulent fluctuation. Based on Morkovin's hypothesis, we use wall friction velocity and density to the dimensionless turbulent fluctuation. The current results are in good agreement with previous incompressible results,[53,54] and the fluctuation intensity in the three directions in the near-wall region has a strong anisotropy, demonstrating the accuracy of the current LES results.

III. RESULT

A. Flow visualization

According to the definition of Simpson,[12] the fraction of time that the flow moves downstream γ_u can be used to illustrate the degree of separation of the flow field. When $\gamma_u = 0.01$, it means that the flow is incipient detachment (ID); when $\gamma_u = 0.2$, it is intermittent transitory detachment (ITD); when $\gamma_u = 0.5$, it is transitory detachment (TD); when $\gamma_u > 0.5$, it can be considered as detachment (D). Figure 5 shows the distribution of γ_u along the streamwise direction at the wall. For the case of $34°$, γ_u in most areas of the interaction zone is greater than 0.5, meaning that the flow has separated. It can be seen that the peak of γ_u is greater than 0.5 for the case of $14°$, which is a normal phenomenon. Since the Simpson criterion is defined based on the fraction of time that the flow moves downstream, there is a certain probability that the incipiently separated flow field is separated at the corner point while remaining attached elsewhere. Settles *et al.*[39] pointed out that some tiny separated regions are always present, even for very low corner angles. So it is normal to have the likelihood of separation at the corner point. It can also be seen from the skin friction coefficient in Fig. 7 that the separation bubble of the $14°$ is tiny, which
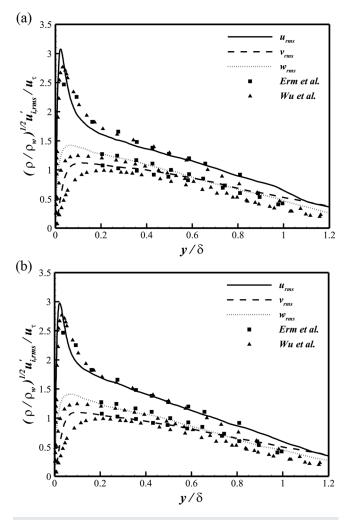

FIG. 4. Profiles of density-weighted turbulence intensities of three velocity fluctuation components for the two cases: (a) incipient separation and (b) fully separated flow.

indicates that the currently selected angle is reliable. Figure 6 also shows the contours of mean streamwise velocity fields. It can be seen that the incipiently separated flow field is attached, while the fully separated flow field has an obvious separation bubble. Therefore, in the following discussion, we use incipiently separated and fully separated flow to represent these two cases.

The streamwise distributions of mean wall pressure and skin friction coefficient are shown in Fig. 7. The wall pressure first rises sharply due to the separation shock, followed by a plateau due to the separation of the flow, and further rises downstream due to the reattachment shock. When comparing the pressure distribution of the incipient and fully separated flow, it can be shown that the incipient separation case has a smaller separation bubble, which results in a smaller pressure plateau than the fully separated case. This phenomenon can also be seen in the distributions of skin friction. The overshoot of wall pressure and skin friction of fully separated flow is larger than that of incipient separation.

FIG. 5. The distribution of γ_u along the streamwise direction at the wall.
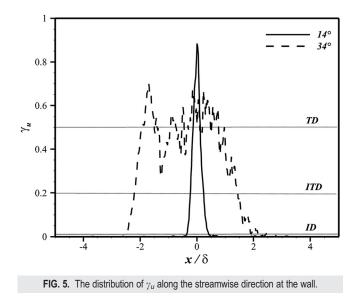
Figure 8 shows the instantaneous temperature contours of the midspan under the two conditions. The fully developed turbulent produces shock waves due to the existence of corner, and the shock wave causes a sudden change in downstream temperature. A local high temperature zone appears in the interaction zone. For the incipiently separated flow, the temperature in the boundary layer of the interaction zone is smaller, and there is almost no separation in the flow field. For the fully separated flow, the separation shock moves upstream, the shock intensity enhances simultaneously, and there is an obvious separation bubble in the flow field. In the downstream reattachment region of the fully separated flow, there is also a local peak wall temperature phenomenon, which will endanger the spacecraft and is one of the problems that the academic community is committed to solving.

Figure 9 shows the map of instantaneous numerical density schlieren for the two cases. The density schlieren map is obtained by
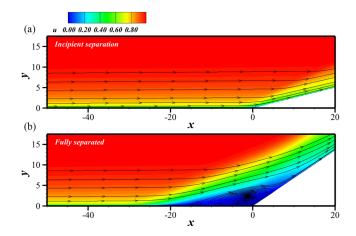

FIG. 7. Distributions of (a) mean wall pressure and (b) skin friction coefficient for the two cases.

FIG. 6. Contours of mean streamwise velocity fields in the x–y plane for the two cases: (a) incipient separation and (b) fully separated flow.
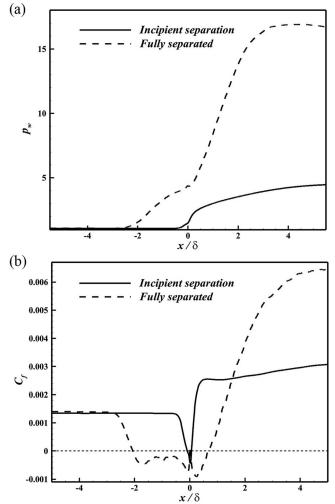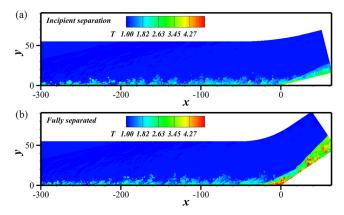

FIG. 8. Contours of instantaneous temperature contours in the midspan ($z = 12$) for the two cases: (a) incipient separation and (b) fully separated flow.
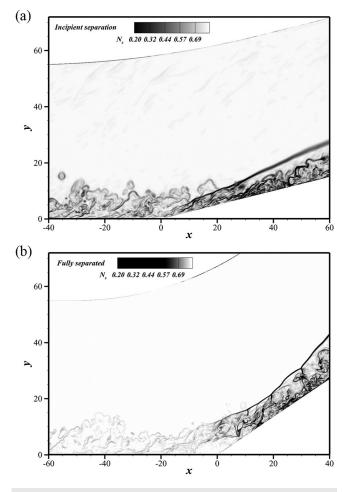
FIG. 9. Instantaneous numerical density schlieren for the two cases: (a) incipient separation and (b) fully separated flow.

FIG. 10. Contours of instantaneous skin-friction coefficient distribution for the two cases: (a) incipient separation and (b) fully separated flow.

calculating the density gradient, where a larger density gradient indicates that the flow is more compressive. We characterize the density gradient in the flow by employing the variable N_s, which is defined as follows:

$$N_s = 0.8 \exp\left(-10 \frac{|\nabla\rho| - |\nabla\rho|_{\min}}{|\nabla\rho|_{\max} - |\nabla\rho|_{\min}}\right). \tag{31}$$

The flow upstream of the corner exhibits ups and downs due to the raised hairpin vortex's slow expansion and breakup. Around the corner, the shock foot of the main shock penetrated the outer edge of the turbulent boundary layer and weakened into compression waves. After the flow passes through the main shock, the compressibility rises quickly in both cases.

The contours of instantaneous skin-friction coefficient distribution are given in Fig. 10. The fully separated flow shows that the skin-friction structures are homogeneously distributed upstream of the corner with streamwise elongated streaky structures. The streaky structures in the separation region are broken due to the significant reverse flow. After reattachment, the streaky structures recover again
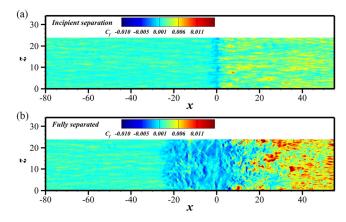
and exhibit a spanwise alternation of high and low velocity structure, which previous studies suggest may be related to the Görtler-like vortices.[6,24] For the incipient separation case, since the flow is less disturbed by the shock, the flow field is almost not separated, so the streaky structures are almost not broken, and the downstream reattachment zone is less affected.

B. Turbulence properties

To reveal the effect of incipient and fully separated on turbulence evolution, we further discuss turbulence properties in terms of Reynolds stress tensor components and turbulent kinetic energy transport equation at different streamwise locations.

Figure 11 shows the contours of the Favre averaged Reynolds stress components $\sqrt{\{u''u''\}}$, $\sqrt{\{v''v''\}}$, $\sqrt{\{w''w''\}}$, where $\{\cdot\}$ denotes the Favre average and the double prime $''$ denotes the turbulent fluctuations with respect to the Favre average. Across the interaction zone, the streamwise turbulence amplified sharply, and the peak is more than twice that of the upstream undisturbed region. For the case of incipient separation, the peak of the turbulence amplification is mainly concentrated at the corner, and the turbulence amplification gradually decreases not far downstream of the corner. Compared with incipient separation, the turbulence amplification range of fully separated flow is expanded at least twice, and the peak appears in $x = -20$. As it develops downstream, the peak gradually decreases and moves out of the boundary layer. As it develops further downstream, the turbulence amplification gradually decreases to the level of the upstream undisturbed region. This phenomenon is consistent with the results of Fang et al.,[55] who pointed out that the main feature of Reynolds stress components amplification is the outward shift of the peak from the near-wall region to the core of the free shear layer or mixing layer. The contours show a greater difference in v''_{rms}. For the case of incipient separation, the peak occurs at the base of the main shock, and there is a small amplification in the near-wall region starting from $x = -19$, which continues downstream of the corner. The amplification range becomes larger near the corner region. Two local peaks occur in the contours of v''_{rms} of fully separated flow, one occurs in the near-wall region near the separation point, and the other coincides with the
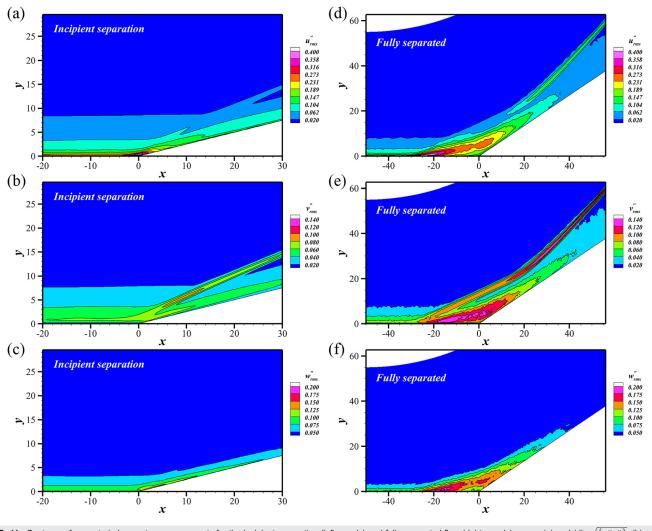
FIG. 11. Contours of mean turbulence stress components for the incipient separation (left panels) and fully separated flow (right panels) cases: (a) and (d) $\sqrt{\{u''u''\}}$; (b) and (e) $\sqrt{\{v''v''\}}$; and (c) and (f) $\sqrt{\{w''w''\}}$.

main shock. The first peak moves from the near-wall region to the free shear layer as it develops downstream, with the same trend as u''_{rms}. The second peak is at the center of the main shock, and the amplification decreases gradually from the center along the shock outward. The w''_{rms} of incipient separation without significant amplification. For fully separated flow, the trend of the w''_{rms} is the same as u''_{rms}, but the intensity weakens.

In Fig. 12, the profiles of Reynolds stress components $R_{11} = \langle \rho u'' u'' \rangle$, $R_{22} = \langle \rho v'' v'' \rangle$, $R_{33} = \langle \rho w'' w'' \rangle$ along the wall-normal direction at different positions are shown, where $\langle \cdot \rangle$ is the Reynolds averaging, and prime $'$ denotes the turbulent fluctuations with respect to the Reynolds average. The results exhibit similarities with previous findings.[56–59] For the case of incipient separation, when at the corner, R_{11} increases significantly, and the peak is slightly shifted out of the boundary layer, and when reaching the downstream reattachment boundary layer, R_{11} shows a double-peaked structure. The R_{22} and R_{33}

show the same trend at the upstream undisturbed region and the corners, but after reattachment, R_{22} slowly increases and peaks in the outer zone. In contrast, R_{33} increases rapidly to peak within the boundary layer. At the outer edge of the boundary layer, there is a spike in R_{22}, which may be caused by the penetration of the main shock into the boundary layer. R_{12} also increases rapidly as it enters the corner to reach the downstream reattachment boundary layer, with the difference that the value of R_{12} in the outer zone of the boundary layer gradually becomes less than zero as it progresses downstream. For the case of fully separated, the growth trend of Reynolds stress components is the same. From the upstream undisturbed region to the downstream, the value of Reynolds stress components increases rapidly, and the peak gradually moves outside the boundary layer. Fang *et al.*[55] pointed out that when entering the interaction zone, the peaks moving away from the wall indicate there is a creation of a detached free shear layer. With the slow damping of the
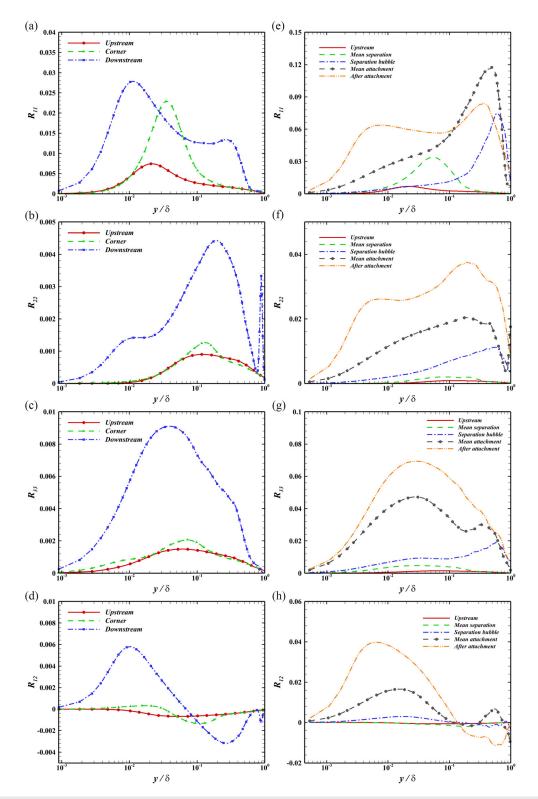
FIG. 12. Distributions of the Reynolds stress components at various streamwise locations for the incipient separation (left panels) and fully separated flow (right panels) cases: (a) and (e) R_{11}; (b) and (f) R_{22}; (c) and (g) R_{33}; and (d) and (h) R_{12}.

Reynolds stress incident, the free shear layer starts to decay and diffuse after being developed. During this process, R_{12} also gradually grows to peak in the boundary layer and then collapses and falls to negative in the outer region of the boundary layer.

Furthermore, Reynolds stress invariants can represent the intrinsic characteristics of Reynolds stress. The anisotropy tensor of the Reynolds stress is defined as[60]

$$b_{ij} = \frac{\widetilde{u_i'' u_j''}}{2k} - \frac{1}{3}\delta_{ij}, \qquad (32)$$

where $k = \widetilde{u_i'' u_i''}/2$. The three independent invariants I, II, and III of the anisotropy tensor are given by

$$I = 0, \quad II = -\frac{b_{ij}b_{ji}}{2}, \quad III = \frac{b_{ij}b_{jk}b_{ki}}{3}. \qquad (33)$$

For convenience, we use variables η and ξ to form a Lumley triangle to characterize the state of anisotropy, where η and ξ are defined as follows:[60]

$$\xi^3 = \frac{III}{2}, \quad \eta^2 = -\frac{II}{3}. \qquad (34)$$

Figure 13 displays the anisotropy invariant maps for two cases at various streamwise locations. The origin of the triangle in Fig. 13 represents the isotropic turbulence. The top left and right corners represent the turbulence at two-component axisymmetric and one-component states, respectively. The straight sides at the bottom left and right represent the axisymmetric compression and axisymmetric expansion states, respectively, and the top curve represents two-component turbulence. Because of the blocking effect, the computed anisotropy curve in the upstream undisturbed region shows a two-component turbulence close to the wall.[51] At the outer edge of the boundary layer, the flow in both cases tends to the state of axisymmetric expansion. However, when entering the interaction region and reaching the corner, the anisotropy invariant maps of the two cases change significantly. The turbulence states are consistent with the upstream undisturbed region for the incipient separation. Due to the strong adverse pressure gradient in the fully separated flow, the turbulence near the wall tends to the two-component axisymmetric state, while the turbulence at the outer edge of the boundary layer is in the state of axisymmetric expansion. The turbulence within the boundary layer tends to axisymmetric compression. Interestingly, as the flow progresses downstream, the anisotropy of the turbulence under the incipient separation gradually decreases, and some of the flow tends to be axisymmetric compression. The near-wall turbulence under fully separated flow returns to a two-component turbulence state.

Turbulent kinetic energy (TKE) is an important physical quantity in the flow field, and the TKE transport equation is important for studying the TKE budget.

TKE budget for compressible in LES could be briefly described as follows:[61]

$$\frac{\partial \bar{\rho}k}{\partial t} = P + T + V - D + C + K + M + SGS, \qquad (35)$$

where $\widetilde{k} = \frac{1}{2}\frac{\overline{\rho u_i'' u_i''}}{\bar{\rho}}$ is TKE. Table II shows more details for each term. Both the viscous diffusion and the viscous dissipation are functions of
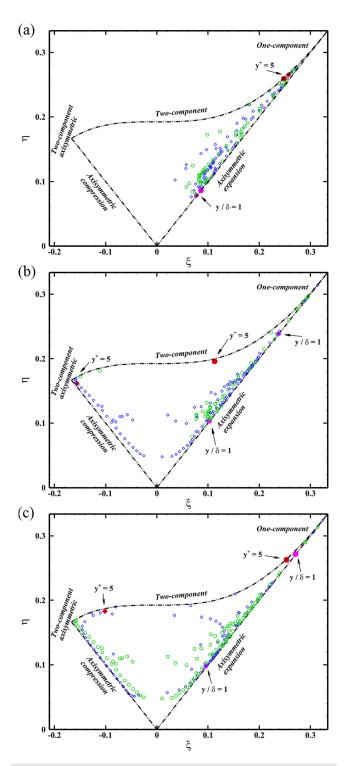

FIG. 13. Lumley triangles for wall-normal profiles (a) in the upstream undisturbed region, (b) at the corner, and (c) at the downstream. Green open circle: incipient separation; blue open square: fully separated flow; red solid circle: incipient separation at $y^+ = 5$; red solid square: fully separated flow at $y^+ = 5$; pink solid circle: incipient separation at $y/\delta = 1$; and red solid square: fully separated flow at $y/\delta = 1$.

TABLE II. Expression for the terms in the TKE budget equation.

Expression	Meanings
$P = -\overline{\rho u_i'' u_j''}\, \partial \widetilde{u}_j / \partial x_j$	Turbulent production
$T = -\partial (1/2 \overline{\rho u_i'' u_i'' u_j''} + \overline{p' u_j''}) / \partial x_j$	Turbulent transport
$V = \partial \overline{\sigma_{ij}' u_i''} / \partial x_j$	Viscous diffusion
$D = \overline{\sigma_{ij}' \partial u_i'' / \partial x_j}$	Viscous dissipation
$C = -\partial \overline{\rho}\, \widetilde{u}_j k / \partial x_j$	Convection
$K = \overline{p' \partial u_i'' / \partial x_i}$	Pressure dilation
$M = \overline{u_i''} (\partial \overline{\sigma}_{ij} / \partial x_j - \partial \overline{p} / \partial x_i)$	Compressible mass terms
$\mathrm{SGS} = \partial \langle \tau_{ij} u_i'' \rangle / \partial x_j + \langle \tau_{ij} \partial u_i'' / \partial x_j \rangle$	Diffusion and dissipation in sgs

the shear stress tensor, which, for an LES solution, includes both the resolved stress σ_{ij} and the unresolved SGS stress τ_{ij}.

In the upstream undisturbed region, the sum of all the terms on the right-hand side of Eq. (35) has been evaluated, and it is also shown in Fig. 14 as a dotted line. The local balance of TKE is very close to zero, indicating an accurate prediction of the right-hand contributions. The SGS terms in Fig. 14 are calculated as the remainder of the sum of all other budget terms and represent the combined contribution of the SGS diffusion and SGS dissipation terms. Morgan and Lele[62,63] confirmed that when the grid resolution of the LES reaches a certain level ($\Delta x^+ \leq 30$, $\Delta y^+ \leq 1$, and $\Delta z^+ \leq 15$), the distribution of the terms of the TKE transport equation is similar to that of the DNS, and the results of the numerical simulations are almost the same. So the contribution of the SGS terms in Fig. 14 is almost zero, probably because the grid resolution is very high. From the figure, we can see that in both cases in the near-wall area, the TKE is mainly transported from the area far away from the wall to the wall by the turbulent production term P through the turbulent transport term T and then diffused and dissipated by the viscosity. We can also see that in the STBLI, turbulent transport term T, turbulent production term P, viscous diffusion V, and viscous dissipation D are important physical quantities that affect the transport process of TKE in the interaction region. So we mainly focus on the distribution of these items.

At the compression corner, in the case of incipient separation, the peaks of the TKE transport equation's main terms change sharply, see Fig. 15. The peak of turbulent production increased more than doubled, and the transport term increased to a positive value in $y^+ = 20$ and then reached the peak at $y^+ = 28$. The trend is consistent with the upstream undisturbed region in general. However, the case of fully separated has changed a lot. With away from the wall, the turbulent production is further increased, and the first peak occurs at $y^+ = 330$, then begins to decrease until $y^+ = 512$, and then increases again to a peak at $y^+ = 503$. The turbulence transport term is increased to balance the convection term in the near wall.[61] Increases in turbulence transport mainly balance the increase in production in the separation shear layer. During this process, the contribution of viscous is minimal.

Overall, the incipient separation is almost restored to the upstream undisturbed region in the downstream boundary layer, see Fig. 16. However, for the fully separated flow, the production, transport, and viscous terms are increased significantly at the wall due to
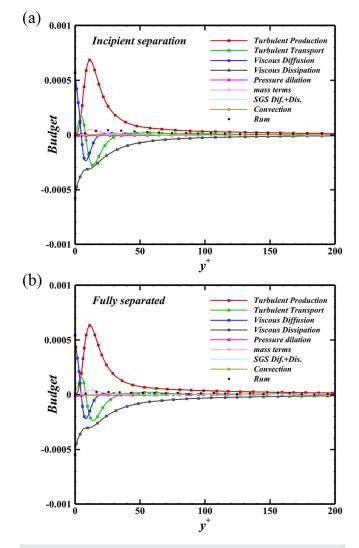

(a)

(b)

FIG. 14. Main terms of the TKE budget in the upstream undisturbed region for the two cases: (a) incipient separation and (b) fully separated flow.

the strength of the mean shear in this region. It also shows that the effect of the shock wave has yet to be eliminated.

C. Vortex structure

Coherent structure, also known as vortical structure, is an essential feature of turbulent motion. Various scales of vortical structures exist in turbulence, including small eddies with a random motion to relatively organized large-scale vortex structures. Although studying the properties of turbulence can help us understand the correlations and general average information in the flow, we need a more direct understanding of the formation, growth, interaction, and dissipation of vortices. Therefore, studying the evolution of the coherent structure can help us understand the evolution characteristics of the flow field more deeply and compare the effects of different separation conditions on the STBLI.
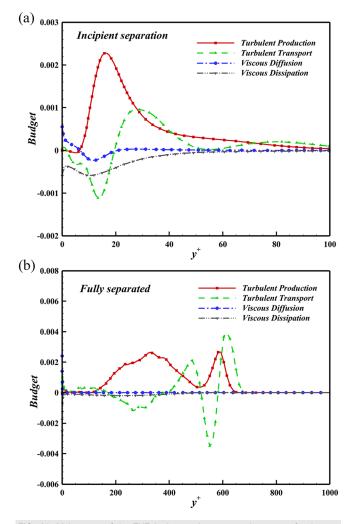
FIG. 15. Main terms of the TKE budget at the compression corner for the two cases: (a) incipient separation and (b) fully separated flow.

FIG. 16. Main terms of the TKE budget in the downstream boundary layer for the two cases: (a) incipient separation and (b) fully separated flow.

There are various criteria for identifying the vortex structure,[64–66] and in this paper, we use the Q criterion, which is the second invariant of the velocity gradient tensor,[64]

$$Q = -\frac{1}{2}\left(S_{ij}S_{ij} - W_{ij}W_{ij}\right), \tag{36}$$

$$S_{ij} = \frac{1}{2}\left(\frac{\partial u_i}{\partial x_j} + \frac{\partial u_j}{\partial x_i}\right), \tag{37}$$

$$W_{ij} = \frac{1}{2}\left(\frac{\partial u_i}{\partial x_j} - \frac{\partial u_j}{\partial x_i}\right). \tag{38}$$

The three-dimensional coherent vortex structure identified using the Q criterion is given in Fig. 17, colored by the local streamwise velocity u, where the threshold $Q = 0.1$. It can be seen that there are a large number of coherent structures within the boundary layer.

The distribution of the vortex structure in the upstream and at the corner for the incipient separation case is given in Fig. 18. Near the wall,
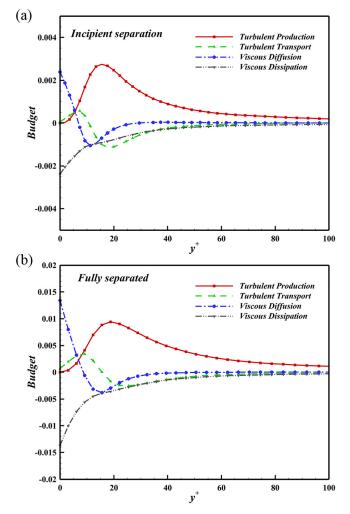
the vortex structure is dominated by densely distributed quasi-flow vortices, which gradually lift upward and increase as they move away from the wall. The vortex structures are densely distributed at the corner, forming larger-scale hairpin vortex strings or package structures.

Figure 19 shows the vortex structure at different positions of the fully separated flow. The vortex structure has the same distribution with incipient separation in the upstream region. However, when entering the interaction region, the flow field generates a strong reverse pressure gradient due to the shock wave, which causes the boundary layer after the shock to thicken, and finally leads to the vortex structures growing rapidly. In addition, due to the action of the shock wave, the flow field exhibits a strong three-dimensional effect, and a chaotic vortex structure distribution appears in the flow field downstream of the corner.

Although the Görtler structure can hardly be called a single vortex from the definition of vortex, it still plays an important role in the STBLI.[6,24,67] The Görtler number is defined as
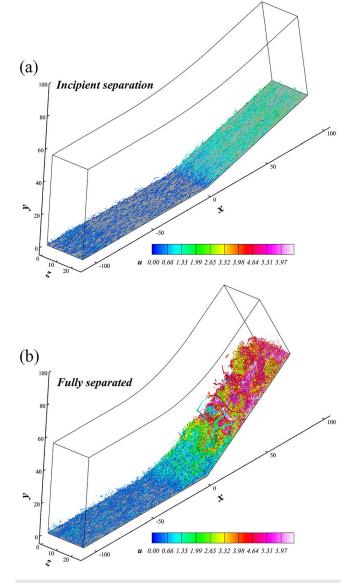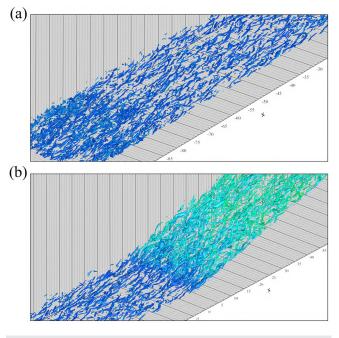
08 April 2024 03:03:04

FIG. 17. Three-dimensional coherent vortex structure identified using the *Q* criterion for the two cases: (a) incipient separation and (b) fully separated flow.

$$G_T = \frac{\theta}{0.018\delta^*}\sqrt{\frac{\theta}{R}}, \qquad (39)$$

where θ and δ^* correspond to the momentum thickness and displacement thickness of the turbulent boundary layer at the inlet of the corner, and R is the radius of curvature of the corner flow.

The critical Görtler number in the laminar flow is 0.6, while the validity of the Görtler stability criterion is unclear in a turbulent and separated flow.[59] However, according to a previous research, a higher Görtler number can also be regarded as evidence of the existence of Görtler structures in the flow field.[24,59,67] Figure 20 shows the distribution of Görtler number along the mean streamlines in the corner of the two cases. The starting point of the mean streamline is taken at

FIG. 18. Vortex structure of incipient separation (a) in the upstream and (b) at the corner.

$y/\delta = 0.3$ at the inlet of the corner. It can be seen that the Görtler number has only one peak in the case of incipient separation, but it shows a bimodal distribution under fully separated flow. This is mainly due to the different sizes of the separation bubble in the two cases, resulting in different local curvatures in the case of the same wall-normal height. In addition, their peak all exceeds the threshold of the Görtler number, indicating there exist Görtler structures in the flow field.

D. Low frequency unsteadiness

Under the influence of STBLI, the flow will separate, resulting in a separation bubble and shock. The separation shock foot oscillates back and forth over the intermittent region, accompanied by the expansion and contraction of the separation bubble. The characteristic frequency of this unsteady phenomenon is usually one to two orders of magnitude lower than the characteristic frequency of turbulent fluctuation in the incoming boundary layer. This phenomenon is called the low-frequency unsteadiness of STBLI.[10,68] Nowadays, there are still entirely different physical explanations for the low-frequency unsteadiness of STBLI in the academic world. Therefore, studying the oscillation characteristics of separation shock will help further understand the relevant mechanism of the unsteady motion of the separation shock.

Figure 21 shows the power spectral density of the wall pressure fluctuations at the upstream undisturbed region $P1$ and the mean separation point $P2$. For the case of incipient separation, since the flow field hardly generates shock waves, the frequency of the wall pressure fluctuation in the upstream undisturbed region of the flow is almost the same as that at the mean separation point. However, for the case of fully separated flow, in the upstream undisturbed region, the peak
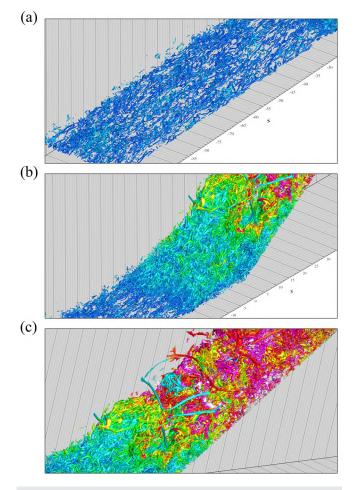
FIG. 19. Vortex structure of fully separated flow (a) in the upstream, (b) in the inter-action region, and (c) downstream of the corner.

FIG. 20. Distribution of Görtler numbers along the mean streamline.

frequency of the wall pressure fluctuation is located near $f\delta/U_\infty = 1$. At the mean separation point, the low-frequency energy of the wall pressure fluctuations rises rapidly, and a peak frequency appears at $f\delta/U_\infty < 0.1$.

Figure 22 shows the distribution of the energy spectrum of DMD with frequency. The results show that for the fully separated flow, the energy is mainly concentrated in the low-frequency modes, and the energy in the high-frequency modes is relatively low. Although there is a small amount of energy at low frequencies for the incipient separation, the overall energy distribution is uniform.

IV. CONCLUSION

In the present study, large eddy simulation of shock wave and hypersonic turbulent boundary layer interaction on a compression ramp at the Mach number $Ma_\infty = 5$ and Reynolds number $Re_\infty = 14\,000$ is performed to investigate the influence of the incipient and fully separated conditions on the flow field evolution. The definition of incipient and fully separated flow is deepened by the Simpson criterion and mean velocity contour. Two compression ramp angles, 14° and 34° corresponding to the incipiently separated and fully separated, are
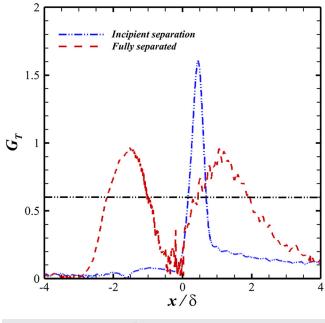
considered; in the incipiently separated flow, there is almost no separation in the flow, while in the fully separated flow, a separation bubble is observed.

A quasi-dynamic subgrid-scale kinetic energy equation model has been applied, which combines the merits of the eddy-viscosity model and the gradient model, and the local coefficients of the model are determined dynamically. The distribution of the van Direst transformed mean streamwise velocity and the root mean square of the velocity components are compared against previous incompressible experimental and numerical results, and a satisfactory agreement is achieved.

The mean wall pressure and skin friction coefficient indicate that the incipient separation flow field is attached, while the fully separated flow field has an obvious separation bubble. The instantaneous temperature contours show strong local peak wall temperature in the interaction and reattachment region of the fully separated flow. However, there is no such phenomenon in the incipiently separated flow.

In both cases, the contours of the Reynolds stress components exhibit significant amplification in the interaction zone, and the peak outward shifts from the near-wall region to the core of the free shear layer. However, the intensity of the amplification of the fully separated flow is significantly greater than that of the incipient separation. The profiles of Reynolds stress components also show the same trend, in which the free shear layer is detached, decayed, and diffused. The incipient separation trend of TKE items in different streamwise locations is similar, but the peak value has increased more than doubled. The turbulent production and turbulent diffusion change significantly in the fully separated case.

The coherent vortex structures are analyzed using the Q criterion. In both cases, the vortex structure increases in the interaction region. In the case of incipient separation, the vortex structure is not disturbed
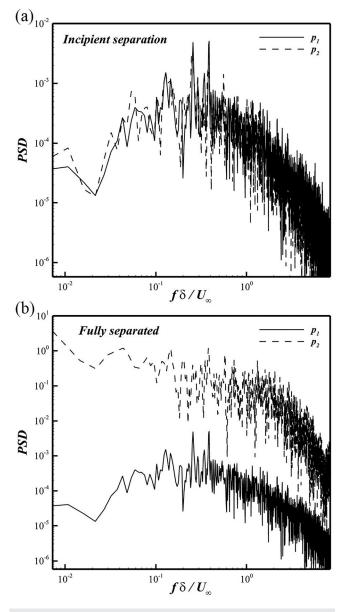
(a)

(b)

FIG. 21. Power spectral density of the wall pressure fluctuations for the two cases: (a) incipient separation and (b) fully separated flow.

FIG. 22. Distribution of DMD mode energy with frequencies for the two cases: (a) incipient separation and (b) fully separated flow.

AUTHOR DECLARATIONS

Conflict of Interest

The authors have no conflicts to disclose.

Author Contributions

Xiangxin Ji: Writing – original draft (equal). **Xinliang Li:** Resources (equal); Software (equal); Writing – review & editing (equal). **Fulin Tong:** Methodology (equal); Writing – review & editing (equal). **Changping Yu:** Supervision (equal); Writing – review & editing (equal).

DATA AVAILABILITY

The data that support the findings of this study are available within the article.

REFERENCES

[1]D. S. Dolling, "Fifty years of shock-wave/boundary-layer interaction research: What next?," AIAA J. **39**(8), 1517–1531 (2001).

[2]D. S. Dolling and M. T. Murphy, "Unsteadiness of the separation shock wave structure in a supersonic compression ramp flowfield," AIAA J. **21**(12), 1628–1634 (1983).

[3]M. S. Selig, J. Andreopoulos, K. C. Muck, J. P. Dussauge, and A. J. Smits, "Turbulence structure in a shock wave/turbulent boundary-layer interaction," AIAA J. **27**(7), 862–869 (1989).

[4]M. E. Erengil and D. S. Dolling, "Unsteady wave structure near separation in a Mach 5 compression rampinteraction," AIAA J. **29**(5), 728–735 (1991).

[5]D. E. Samper and G. Chandola, "Separated shear layer effect on shock-wave/turbulent-boundary-layer interaction unsteadiness," J. Fluid Mech. **848**, 154–192 (2018).

by the shock. In contrast, in the case of fully separated, the flow shows strong three-dimensional characteristics due to the strong reverse pressure gradient generated by the shock, and the distribution of the vortex structure is disordered. We also found Görtler structures in the flow field through instantaneous skin-friction coefficient distribution and Görtler number.

The power spectral density of the wall pressure fluctuations shows that the low-frequency motion of the incipient separation is not apparent. In contrast, the fully separated flow shows an apparent low-frequency phenomenon. The DMD result showed that the energy in both cases is mainly concentrated in the low-frequency modes.
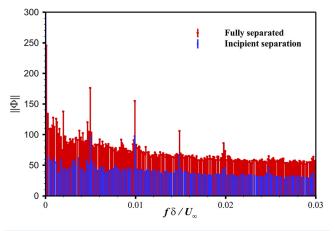
[6]W. B. Hu, S. Hickel, and B. W. van Oudheusden, "Low-frequency unsteadiness mechanisms in shock wave/turbulent boundary layer interactions over a backward-facing step," J. Fluid Mech. **915**, 34 (2021).

[7]F. Tong, S. Dong, J. Duan, X. Yuan, and X. Li, "Effect of expansion on the wall heat flux in a supersonic turbulent boundary layer," Phys. Fluids **34**(10), 105109 (2022).

[8]F. Tong, X. Li, X. Yuan, and C. Yu, "Incident shock wave and supersonic turbulent boundarylayer interactions near an expansion corner," Comput. Fluids **198**, 104385 (2020).

[9]V. D. Gaitonde, "Progress in shock wave/boundary layer interactions," in 43rd Fluid Dynamics Conference, 2013.

[10]N. T. Clemens and V. Narayanaswamy, "Low-frequency unsteadiness of shock wave/turbulent boundary layer interactions," Annu. Rev. Fluid Mech. **46**(1), 469–492 (2014).

[11]R. L. Simpson, J. H. Strickland, and P. W. Barr, "Features of a separating turbulent boundary layer in the vicinity of separation," J. Fluid Mech. **79**(3), 553–594 (1977).

[12]R. L. Simpson, "Turbulent boundary-layer separation," Annu. Rev. Fluid Mech. **21**(1), 205–232 (1989).

[13]M. Wu and M. P. Martín, "Analysis of shock motion in shockwave and turbulent boundary layer interaction using direct numerical simulation data," J. Fluid Mech. **594**, 71–83 (2008).

[14]F. Tong, C. Yu, Z. Tang, and X. Li, "Numerical studies of shock wave interactions with a supersonic turbulent boundary layer in compression corner: Turning angle effects," Comput. Fluids **149**, 56–69 (2017).

[15]B. John and V. Kulkarni, "Effect of leading edge bluntness on the interaction of ramp induced shock wave with laminar boundary layer at hypersonic speed," Comput. Fluids **96**, 177–190 (2014).

[16]J. Duan, X. Li, X. Li, and H. Liu, "Direct numerical simulation of a supersonic turbulent boundary layer over a compression–decompression corner," Phys. Fluids **33**(6), 065111 (2021).

[17]Z. Xie, Z. Xiao, G. Wang, and Y. Yang, "Direct numerical simulation of the effects of Reynolds number in Mach 2.9 flows over an expansion–compression corner," Phys. Fluids **34**(12), 125129 (2022).

[18]J. Zhang, T. Guo, G. Dang, and X. Li, "Direct numerical simulation of shock wave/turbulent boundary layer interaction in a swept compression ramp at Mach 6," Phys. Fluids **34**(11), 116110 (2022).

[19]S. J. Beresh, N. T. Clemens, and D. S. Dolling, "Relationship between upstream turbulent boundary-layer velocity fluctuations and separation shock unsteadiness," AIAA J. **40**(12), 2412–2422 (2002).

[20]B. Ganapathisubramani, N. T. Clemens, and D. S. Dolling, "Large-scale motions in a supersonic turbulent boundary layer," J. Fluid Mech. **556**, 271–282 (2006).

[21]B. Ganapathisubramani, N. T. Clemens, and D. S. Dolling, "Low-frequency dynamics of shock-induced separation in a compression ramp interaction," J. Fluid Mech. **636**, 397–425 (2009).

[22]S. Pirozzoli and F. Grasso, "Direct numerical simulation of impinging shock wave/turbulent boundary layer interaction at M = 2.25," Phys. Fluids **18**(6), 065113 (2006).

[23]S. Piponniau, J. P. Dussauge, J. F. Debiève, and P. Dupont, "A simple model for low-frequency unsteadiness in shock-induced separation," J. Fluid Mech. **629**, 87–108 (2009).

[24]S. Priebe, J. H. Tu, C. W. Rowley, and M. P. Martín, "Low-frequency dynamics in a shock-induced separated flow," J. Fluid Mech. **807**, 441–477 (2016).

[25]M. Waindim, L. Agostini, L. Larchêveque, M. Adler, and D. V. Gaitonde, "Dynamics of separation bubble dilation and collapse in shock wave/turbulent boundary layer interactions," Shock Waves **30**(1), 63–75 (2020).

[26]W. Hu, S. Hickel, and B. W. van Oudheusden, "Unsteady mechanisms in shock wave and boundary layer interactions over a forward-facing step," J. Fluid Mech. **949**, A2 (2022).

[27]X. Li, Y. Zhang, H. Yu, Z. Lin, H. Tan, and S. Sun, "Görtler vortices behavior and prediction in dual-incident shock-wave/turbulent-boundary-layer interactions," Phys. Fluids **34**(10), 106103 (2022).

[28]C. S. Combs, J. D. Schmisseur, B. F. Bathel, and S. B. Jones, "Analysis of shock-wave/boundary-layer interaction experiments at Mach 1.8 and Mach 4.2," AIAA Paper No. 2019-0344, 2019.

[29]Y. Zhou, Y. Zhao, Y. Zhao, G. He, and P. Gao, "Investigation on conical separation vortex generated by swept shock wave/turbulent boundary layer interaction," Acta Astronaut. **199**, 103–112 (2022).

[30]N. Tonicello, G. Lodato, and L. Vervisch, "Turbulence kinetic energy transfers in direct numerical simulation of shock-wave–turbulence interaction in a compression/expansion ramp," J. Fluid Mech. **935**, A31 (2022).

[31]J. Shi and H. Yan, "Turbulence amplification in the shock wave/turbulent boundary layer interaction over compression ramp by the flux reconstruction method," Phys. Fluids **35**(1), 016122 (2023).

[32]F. Tong, S. Dong, J. Lai, J. X. Yuan, and X. Li, "Wall shear stress and wall heat flux in a supersonic turbulent boundary layer," Phys. Fluids **34**(1), 015127 (2022).

[33]F. Tong, J. Lai, J. Duan, S. Dong, X. Yuan, and X. Li, "Effect of interaction strength on recovery downstream of incident shock interactions," Phys. Fluids **34**(12), 125127 (2022).

[34]F. Tong, X. Yuan, J. Lai, J. Duan, D. Sun, and S. Dong, "Wall heat flux in a supersonic shock wave/turbulent boundary layer interaction," Phys. Fluids **34**(6), 065104 (2022).

[35]Z. Jiang, Y. Ji, and J. Wang, "Compressibility effect on interaction of shock wave and turbulent boundary layer," Phys. Fluids **34**(7), 075122 (2022).

[36]J. Lai, Z. Fan, S. Dong, X. Li, F. Tong, and X. Yuan, "Direct numerical simulation of supersonic bump flow with shock impingement," Phys. Fluids **34**(10), 105131 (2022).

[37]T. Guo, J. Fang, J. Zhang, and X. Li, "Direct numerical simulation of shock-wave/boundary layer interaction controlled with convergent–divergent riblets," Phys. Fluids **34**(8), 086101 (2022).

[38]H. Qi, X. Li, R. Hu, and C. Yu, "Quasi-dynamic subgrid-scale kinetic energy equation model for large-eddy simulation of compressible flows," J. Fluid Mech. **947**, A22 (2022).

[39]G. S. Settles, S. M. Bogdonoff, and I. E. Vas, "Incipient separation of a supersonic turbulent boundary layer at high Reynolds numbers," AIAA J. **14**(1), 50–56 (1976).

[40]F. K. Lu, "New results on the incipient separation of shock/boundary-layer interactions," Procedia Eng. **126**, 12–15 (2015).

[41]H. Babinsky and J. Edwards, "On the incipient separation of a turbulent hypersonic boundary layer," Aeronaut. J. **100**(996), 209–214 (1996).

[42]H. Babinsky and J. K. Harvey, *Shock Wave-Boundary-Layer Interactions* (Cambridge University Press, 2011), Vol. 32.

[43]F. W. Spaid and J. C. Frishett, "Incipient separation of a supersonic, turbulent boundary layer, including effects of heat transfer," AIAA J. **10**(7), 915–922 (1972).

[44]G. Coleman and J. Stollery, "Heat transfer from hypersonic turbulent flow at a wedge compression corner," J. Fluid Mech. **56**(4), 741–752 (1972).

[45]G. Elfstrom, "Turbulent hypersonic flow at a wedge-compression corner," J. Fluid Mech. **53**(1), 113–127 (1972).

[46]K. C. Muck and A. J. Smits, "The behaviour of a compressible turbulent boundary layer under incipient separation conditions," in *Turbulent Shear Flows 4* (Springer, 1983), pp. 235–245.

[47]J. L. Steger and R. F. Warming, "Flux vector splitting of the inviscid gasdynamic equations with application to finite-difference methods," J. Comput. Phys. **40**(2), 263–293 (1981).

[48]A. Jameson, W. Schmidt, and E. Turkel, "Numerical solution of the Euler equations by finite volume methods using Runge Kutta time stepping schemes," in 14th Fluid and Plasma Dynamics Conference, 1981.

[49]S. Gottlieb and C. W. Shu, "Total variation diminishing Runge-Kutta schemes," Math. Comput. **67**(221), 73–85 (1998).

[50]X. Li, D. Fu, Y. Ma, and X. Liang, "Direct numerical simulation of shock/turbulent boundary layer interaction in a supersonic compression ramp," Sci. China Phys., Mech. Astron. **53**(9), 1651–1658 (2010).

[51]F. Tong, X. Li, Y. Duan, and C. Yu, "Direct numerical simulation of supersonic turbulent boundary layer subjected to a curved compression ramp," Phys. Fluids **29**(12), 125101 (2017).

[52]T. Fulin, S. Dong, and X. Li, "Direct numerical simulation of impinging shock wave and turbulent boundary layer interaction over a wavy-wall," Chin. J. Aeronaut. **34**(5), 350–363 (2021).

[53]X. Wu and P. Moin, "Direct numerical simulation of turbulence in a nominally zero-pressure-gradient flat-plate boundary layer," J. Fluid Mech. **630**, 5–41 (2009).

[54]L. P. Erm and P. N. Joubert, "Low-Reynolds-number turbulent boundary layers," J. Fluid Mech. **230**, 1–44 (1991).

[55]J. Fang, A. A. Zheltovodov, Y. Yao, C. Moulinec, and R. D. Emerson, "On the turbulence amplification in shock-wave/turbulent boundary layer interaction," J. Fluid Mech. **897**, A32 (2020).

[56]M. Wu and M. P. Martin, "Direct numerical simulation of supersonic turbulent boundary layer over a compression ramp," AIAA J. **45**(4), 879–889 (2007).

[57]S. Priebe, M. Wu, and M. P. Martín, "Direct numerical simulation of a reflected-shock-wave/turbulent-boundary-layer interaction," AIAA J. **47**(5), 1173–1185 (2009).

[58]A. N. Adams, "Direct simulation of the turbulent boundary layer along a compression ramp at $M = 3$ and $Re_\theta = 1685$," J. Fluid Mech. **420**, 47–83 (2000).

[59]M. S. Loginov, N. A. Adams, and A. A. Zheltovodov, "Large-eddy simulation of shock-wave/turbulent-boundary-layer interaction," J. Fluid Mech. **565**, 135–169 (2006).

[60]J. L. Lumley and G. R. Newman, "The return to isotropy of homogeneous turbulence," J. Fluid Mech. **82**(1), 161–178 (1977).

[61]C. M. Helm and M. P. Martín, "Large eddy simulation of two separated hypersonic shock/turbulent boundary layer interactions," Phys. Rev. Fluids **7**(7), 074601 (2022).

[62]B. Morgan, K. Duraisamy, N. Nguyen, S. Kawai, and S. K. Lele, "Flow physics and RANS modelling of oblique shock/turbulent boundary layer interaction," J. Fluid Mech. **729**, 231–284 (2013).

[63]B. Morgan and S. K. Lele, "Turbulence budgets in oblique shockwave/turbulent boundary layer interactions," in *Annual Research Briefs* (Center for Turbulence Research, 2011), pp. 75–86.

[64]C. R. Hunt, A. A. Wray, and P. Moin, "Eddies, streams, and convergence zones in turbulent flows," in Studying Turbulence Using Numerical Simulation Databases, 2. Proceedings of the Summer Program, 1988.

[65]J. Jeong and F. Hussain, "On the identification of a vortex," J. Fluid Mech. **285**, 69–94 (1995).

[66]J. Jeong, F. Hussain, W. Schoppa, and J. Kim, "Coherent structures near the wall in a turbulent channel flow," J. Fluid Mech. **332**, 185–214 (1997).

[67]D. M. Dawson and S. K. Lele, "Large eddy simulation of a three-dimensional compression ramp shock-turbulent boundary layer interaction," in 53rd AIAA Aerospace Sciences Meeting, 2015.

[68]X. Fan, Z. Tang, G. Wang, and Y. Yang, "Review of low-frequency unsteadiness in shock wave/turbulent boundary layer interaction," Acta Aeronaut. Astronaut. Sin. **43**(1), 625917 (2022).

08 April 2024 03:03:04